

Designing Multi-Axis Force–Torque Sensors by Minimizing the Amplitudes of Their Nonlinear Displacements

R. Bekhti

Control and Robotics Laboratory,
Department of Automated Manufacturing
Engineering,
École de Technologie Supérieure,
Montreal, QC H3C 1K3, Canada
e-mail: rachid.bekhti.1@ens.etsmtl.ca

P. Cardou

Department of Mechanical Engineering,
Laval University,
Quebec, QC G1V 0A6, Canada
e-mail: pcardou@gmc.ulaval.ca

V. Duchaine

Control and Robotics Laboratory,
Department of Automated Manufacturing
Engineering,
École de Technologie Supérieure,
Montreal, QC H3C 1K3, Canada
e-mail: vincent.duchaine@etsmtl.ca

Compliant multi-axis force–torque sensors play a crucial role in many emerging robotic applications, such as telemanipulation, haptic devices and human-robot physical interaction. In order to synthesize the compliant architectures at the core of these sensors, several researchers have devised performance indices from mechanism theory. This paper follows the same approach, but includes the innovation of using the changes in the compliant mechanism geometry as a new performance index. Once external forces are applied, the compliant mechanism deviates from its unloaded configuration, and thus, changes in geometry prevent the sensor from exhibiting a linear response. In order to minimize this nonlinear behavior, the potential sources of error are analyzed by applying linear algebra techniques to the expression of the Cartesian force mapping. Two performance indices are then presented and combined. The first index measures the variations of the Jacobian matrix about the unloaded configuration. The second index measures the amplification of the error arising from the joint displacements measurement. The resulting indices can be expressed symbolically, making them easier to evaluate and synthesize. Finally, we apply the performance indices we have developed to simple compliant mechanisms, and discuss the results. [DOI: 10.1115/1.4032401]

1 Introduction

Recent years have seen advances in various fields of robotics, including telemanipulation [1], surgical devices [2], and service robotics [3]. In many of these emerging applications, robots need to interact with their environment—and more than ever before, as robots were breaking out of the industrial settings to which they had traditionally been confined. These changes provide the context for a renewed interest in sensor technologies and their optimization. For robots that need to interact physically with their environment, multi-axis force–torque sensors can be placed on the robot's wrist to measure the forces and torques it generates. This completes the feedback loop used in most of the control schemes for real-time physical interaction.

The literature has emphasized the importance of using parallel mechanical systems to build the compliant mechanisms at the core of multi-axis force–torque sensors. The design of these compliant mechanisms was largely inspired by the kinematic design of six degrees-of-freedom parallel robotic manipulators. Indeed, several authors [4–6] have designed a variety of multi-axis force–torque sensors based on Stewart platforms [7]. When designing a multi-axis force–torque sensor, perhaps the most crucial step is finding the optimum dimensions of the compliant mechanism in order to measure a desired force range with high precision. To this end, a number of performance-evaluation criteria have already been introduced. Uchiyama et al. [8,9] have proposed a systematic design procedure for minimizing the condition number of the compliance matrix of the force–torque sensor. Bicchi [10] has generalized the condition number of the compliance matrix and proposed that this number be the performance index for the design of the sensor's mechanical architecture. Uchiyama and Svinin [4] have proposed an index for evaluating the isotropy of the force–torque sensor as the main indicator of its performance. Ranganath et al. [6] have dealt with the analysis and design

of a Stewart-platform-based force–torque sensor in a near-singular configuration. Also, we have previously published a comprehensive list of performance criteria and design approaches [11].

However, only a few of these performance criteria have considered the changes in geometry to which the compliant mechanism is subjected as it undergoes deformations, and only one study has attempted to evaluate the linearity of the sensor's response to an external wrench. This one study is by Hirose and Yoneda [12], who have pointed out the problem of nonlinear displacements. These authors propose a method by which one can identify the nonlinear characteristics due to the forces and moments applied on an arbitrary compliant structure. The solution taken in this study to reduce the effect of nonlinear displacements is based on a nonlinear calibration technique. However, the calibration step intervenes at a very late stage of the design procedure, which may require further signal processing and recurrent adjustments.

In this paper, we propose a method to minimize these structural errors at an early stage of the force–torque sensor design. This requires that we minimize the errors caused by changes in geometry. This objective sometimes conflicts with the minimization of the errors resulting from the amplification of the joint displacements measurement-noise, by making the sensor near-isotropic. The changes in geometry are further exacerbated by the necessity of using inexpensive displacement sensors so as to keep the overall cost of the sensor low, with the result that the joint displacements must be larger in order to be detected. If we fail to consider the geometry changes that occur as the compliant mechanism is deformed, our final design of force–torque sensor will contain large structural errors. Therefore, to avoid excessive nonlinear calibrations and recalibrations of the sensor, we must minimize the nonlinear displacements caused by forces and moments applied in different directions from the start of the design process. The current study proposes that we take two factors into account when optimizing the sensor's design: changes in geometry, and the amplification of the errors resulting from the displacement sensors at the measured joints. To this end, we present two indices of the changes in geometry and one index of the measurement error

Contributed by the Mechanisms and Robotics Committee of ASME for publication in the JOURNAL OF MECHANICAL DESIGN. Manuscript received July 19, 2015; final manuscript received December 17, 2015; published online January 20, 2016. Assoc. Editor: Oscar Altuzarra.

amplification. We then illustrate the proposed approach with some examples of simple mechanisms, and validate the functionality of our method.

The paper is organized as follows. In Sec. 2, we begin by deriving a mathematical expression of the relationship between the generalized applied forces and the corresponding joint displacements. We then propose two new indices and revisit the condition number. Section 3 describes our approach to multi-objective optimization, which uses multiple indices of performance. We apply this approach to a simple serial-two-link planar mechanism in Sec. 4. We also apply our methodology to a compliant parallel mechanism-based force sensor, composed of a pair of legs with one prismatic joint and two revolute joints (expressed as 2-PRR, [7,13]), and present the ensuing discussion in Sec. 5, before drawing to a close in Sec. 6.

2 Error Analysis

The vast majority of current force–torque sensors operate under the same principle: essentially, an applied force is transformed into a measurable displacement. Our example uses a compliant mechanism loaded by an external wrench, \mathbf{w} , that generates displacements at preselected joints. These displacements are then detected by means of any of the following options: strain gauges, optical sensors [14], inductive displacement sensors [15,16], or CCD elements [17].

We model the compliant mechanism of the multi-axis force–torque sensor as a rigid-link parallel mechanism, with lumped elastic springs at its joints (see Fig. 1). The rigid-link mechanism must have n degrees-of-freedom, where n is the number of generalized forces it is to measure, i.e., force and torque components. Let us also assume that the mechanism is fully parallel, so that all its m legs are serial kinematic chains, and that each of these legs has exactly n joints allowing for n degrees-of-freedom. We assume the displacement of the j th spring from the i th leg to be $q_{i,j}$, whether it is angular or linear. Its corresponding elastic spring is assumed to have a proportionality constant $k_{i,j}$ and a free length $q_{0,i,j}$. In order to estimate the n -dimensional wrench \mathbf{w} , only n of the $m \times n$ compliant joints are equipped with displacement sensors. We make no assumptions regarding the location of these sensors with respect to the other joints.

From these definitions, we form the array of the joint displacements of the i th leg, $\mathbf{q}_i \equiv [q_{i,1} \cdots q_{i,n}]^T$, and, for the complete mechanism, we form $\mathbf{q} \equiv [\mathbf{q}_1^T \cdots \mathbf{q}_m^T]^T$. The corresponding arrays of the spring constants are $\mathbf{k} \equiv [k_{1,1} \cdots k_{m,n}]^T$, and the arrays of the free lengths are $\mathbf{q}_0 \equiv [q_{0,1,1} \cdots q_{0,m,n}]^T$.

Upon defining the matrix $\mathbf{K}_q \equiv \text{diag}(\mathbf{k})$, the potential energy stored in the compliant mechanism may be expressed as

$$V = (1/2)(\mathbf{q} - \mathbf{q}_0)^T \mathbf{K}_q (\mathbf{q} - \mathbf{q}_0) \quad (1)$$

Let the array \mathbf{p} representing a small displacement of the suspended mass (the rigid body) be compatible with the measured wrench \mathbf{w} , so that we may express the work performed by \mathbf{w} as $\mathbf{p}^T \mathbf{w}$. We now have

$$\begin{aligned} \mathbf{w} &= \frac{\partial V}{\partial \mathbf{p}} \\ &= \left(\frac{\partial \mathbf{q}}{\partial \mathbf{p}} \right)^T \frac{\partial V}{\partial \mathbf{q}} \\ &= \left[(\partial \mathbf{q}_1 / \partial \mathbf{p})^T \cdots (\partial \mathbf{q}_m / \partial \mathbf{p})^T \right] \mathbf{K}_q (\mathbf{q} - \mathbf{q}_0) \\ &= \mathbf{H} \mathbf{K}_q (\mathbf{q} - \mathbf{q}_0) \end{aligned} \quad (2)$$

where $\mathbf{H} \equiv [\mathbf{J}_1^T \cdots \mathbf{J}_m^T]$, and $\mathbf{J}_i \equiv \partial \mathbf{p} / \partial \mathbf{q}_i$ is the Jacobian matrix of the serial chain formed by the i th leg.

This last equation was originally obtained by Ref. [18] for a single serial chain, in order to simulate six degree-of-freedom stiffness in a virtual environment. It is placed here to account for fully parallel mechanisms, and to clarify its link with the application of multi-axis force–torque sensors. Note that Eq. (2) represents a nonlinear relationship between \mathbf{w} and \mathbf{q} , as we consider \mathbf{H} to be a function of \mathbf{q} (symbolically, $\mathbf{H} = \mathbf{H}(\mathbf{q})$). Under these conditions, Eq. (2) is the *exact* mathematical description of the force–displacement relationship for the lumped-compliance rigid-link mechanism described above.

As a typical multi-axis force–torque sensor does not have the same measurement ranges and accuracies in all sensitive directions, it becomes difficult to determine the relative importance of these sensitive directions. More academically, this is the classic problem of the dimensionally nonhomogeneous Jacobian matrix, which prevents the addition of its entries. We propose to resolve this problem by a method akin to that of Yoshikawa [19], whereby we normalize the wrench and joint coordinates. The ranges of applied forces and torques that the sensor should be capable of measuring are defined as

$$\mathbf{w}_{\min} \leq \mathbf{w} \leq \mathbf{w}_{\max} \quad (3)$$

where the inequality \leq is taken componentwise. In parallel, we define the ranges of joint displacements as

$$\mathbf{q}_{\min} \leq \mathbf{q} \leq \mathbf{q}_{\max} \quad (4)$$

In practice, these bounds may come from the maximum deformations allowed at the compliant joints, or by the measurement ranges of displacement sensors at these joints. The parameters \mathbf{w}_{\min} , \mathbf{w}_{\max} , \mathbf{q}_{\min} and \mathbf{q}_{\max} will be known in advance by the designer, so the subsequent normalization should pose no problem.

We obtain the normalized generalized forces $\bar{\mathbf{w}}$ by dividing the applied forces by their corresponding ranges, which yields

$$\bar{\mathbf{w}} \equiv \text{diag}(\mathbf{w}_{\max} - \mathbf{w}_{\min})^{-1} (\mathbf{w} - \mathbf{w}_{\min}) \quad (5)$$

Similarly, the normalized joint coordinates $\bar{\mathbf{q}}$ are computed as

$$\bar{\mathbf{q}} \equiv \text{diag}(\mathbf{q}_{\max} - \mathbf{q}_{\min})^{-1} (\mathbf{q} - \mathbf{q}_{\min}) \quad (6)$$

and the normalized free-lengths as

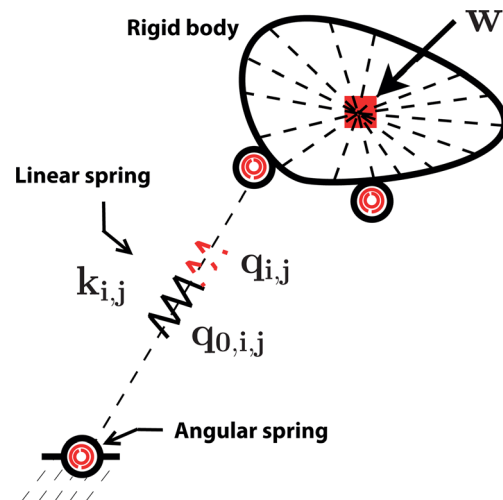


Fig. 1 Generic rigid-link mechanism with lumped elastic springs at its joints

$$\bar{\mathbf{q}}_0 \equiv \text{diag}(\mathbf{q}_{\max} - \mathbf{q}_{\min})^{-1}(\mathbf{q}_0 - \mathbf{q}_{\min}) \quad (7)$$

We substitute Eqs. (5)–(7) into Eq. (2), which yields the normalized relationship

$$\bar{\mathbf{w}} = \bar{\mathbf{H}}\mathbf{K}_q(\bar{\mathbf{q}} - \bar{\mathbf{q}}_0) + \bar{\mathbf{w}}_0 \quad (8)$$

where $\bar{\mathbf{H}} \equiv \text{diag}(\mathbf{w}_{\max} - \mathbf{w}_{\min})^{-1}\mathbf{H}\text{diag}(\mathbf{q}_{\max} - \mathbf{q}_{\min})$ and $\bar{\mathbf{w}}_0 \equiv -\text{diag}(\mathbf{w}_{\max} - \mathbf{w}_{\min})^{-1}\mathbf{w}_{\min}$.

From our initial assumptions, recall that only n of the $m \times n$ joints are equipped with displacement sensors. Symbolically, we thus measure only the variables $\hat{\mathbf{q}} \in \mathbb{R}^n$ out of the variables $\bar{\mathbf{q}} \in \mathbb{R}^{mn}$, and the unmeasured joint displacements are labeled $\check{\mathbf{q}} \in \mathbb{R}^{mn-n}$. The relationship between $\hat{\mathbf{q}}$, $\check{\mathbf{q}}$ and $\bar{\mathbf{q}}$ may therefore be written as

$$\begin{bmatrix} \hat{\mathbf{q}} \\ \check{\mathbf{q}} \end{bmatrix} = \mathbf{P}\bar{\mathbf{q}} = \begin{bmatrix} \hat{\mathbf{P}} \\ \check{\mathbf{P}} \end{bmatrix} \bar{\mathbf{q}} \quad (9)$$

where $\mathbf{P} \in \mathbb{R}^{mn \times mn}$ is a permutation matrix, its submatrices $\hat{\mathbf{P}}$ and $\check{\mathbf{P}}$ possessing n and $mn-n$ rows, respectively. As a permutation matrix is always orthogonal, we may write

$$\bar{\mathbf{q}} = \mathbf{P}^T \begin{bmatrix} \hat{\mathbf{q}} \\ \check{\mathbf{q}} \end{bmatrix} = \hat{\mathbf{P}}^T \hat{\mathbf{q}} + \check{\mathbf{P}}^T \check{\mathbf{q}} \quad (10)$$

From the same reasoning, we obtain $\bar{\mathbf{q}}_0 \equiv \hat{\mathbf{P}}^T \hat{\mathbf{q}}_0 + \check{\mathbf{P}}^T \check{\mathbf{q}}_0$, where $\hat{\mathbf{q}}_0$ and $\check{\mathbf{q}}_0$ are the normalized free-lengths of the springs of the measured and unmeasured joints, respectively. Upon substitution of the latter relationships in Eq. (8), we obtain

$$\bar{\mathbf{w}} = \bar{\mathbf{H}}\mathbf{K}_q\hat{\mathbf{P}}^T(\hat{\mathbf{q}} - \hat{\mathbf{q}}_0) + \bar{\mathbf{H}}\mathbf{K}_q\check{\mathbf{P}}^T(\check{\mathbf{q}} - \check{\mathbf{q}}_0) + \bar{\mathbf{w}}_0 \quad (11)$$

Since the number of degrees-of-freedom of the mechanism, n , is the same as the number of measured joint displacements, one may infer the complete posture from $\hat{\mathbf{q}}$ alone. Therefore, $\check{\mathbf{q}}$ may be seen as a function of $\hat{\mathbf{q}}$ through the mechanism loop-closure equations, i.e., $\check{\mathbf{q}} = \check{\mathbf{q}}(\hat{\mathbf{q}})$.

Hence, the nonlinear relationship of Eq. (2) between \mathbf{w} and \mathbf{q} has been transformed to express the relationship between $\bar{\mathbf{w}}$ and $\hat{\mathbf{q}}$. While still representing the generalized applied forces and joint displacements, respectively, these variables are now expressed in units as percentage points of the scales of their corresponding sensors. Even when coming from different sensors, these percentage points are all summed together to compute the indices proposed in the remainder of this paper. Should the designer require more *relative accuracy* from one sensitive direction than from another, he

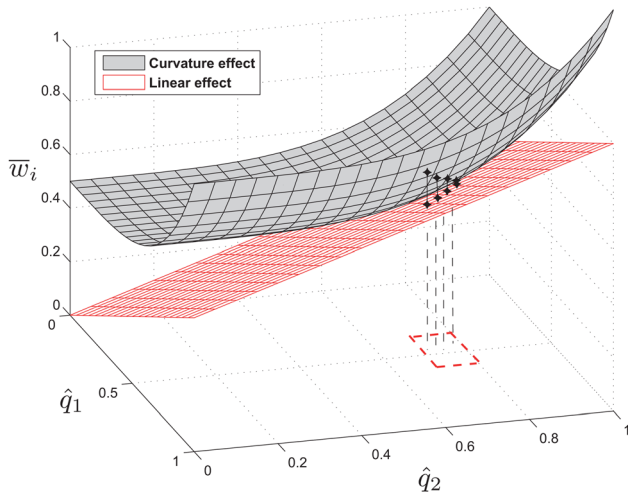


Fig. 2 The nonlinear relationship between \bar{w}_i and \hat{q} , and its linear approximation

or she should modify the proposed normalized coordinates, as the current normalization assumes a *uniform relative sensitivity*.

Figure 2 provides a visualization of the nonlinear relationship between \bar{w}_i , the i th component of $\bar{\mathbf{w}}$, and $\hat{\mathbf{q}}$. In this graph, the force–torque sensor input–output relationship $\bar{w}_i(\hat{\mathbf{q}})$ appears as the curved surface on top, and its linear approximation appears below as a plane. In most existing force–torque sensors, the small ranges of joint displacements $\mathbf{q}_{\min} \leq \mathbf{q} \leq \mathbf{q}_{\max}$ allow for a linear approximation of the nonlinear relationship of Eq. (8), as shown in Fig. 2. However, small ranges of \mathbf{q} require highly sensitive displacement sensors and accurate machining technology, which partly explains the high cost of commercially available force–torque sensors.

Force–torque sensors of lower cost will generally display less sensitivity, requiring larger joint displacements (i.e., a larger distance between \mathbf{q}_{\min} and \mathbf{q}_{\max}) to occur so that they can be detected. The sensors must have a compliant mechanism that can account for the nonlinearity of Eq. (8). While the level of nonlinearity should be minimized, it is also important that the amplification of the joint measurement-error be as lower as possible.

2.1 Change in Geometry. We propose two indices of the importance of nonlinearity in force–torque sensors. The first index takes into account the compliant mechanism behavior over the full range of displacements allowed at its joints. This requires a numerical integration, which is generally computationally intensive. Note also that minimizing just the nonlinearity alone generally leads to a mechanism with high sensitivity to applied forces, as the function $\bar{\mathbf{w}}(\hat{\mathbf{q}})$ tends to approach a constant function. This is undesirable, as it will then take only a small force to produce large displacements at the compliant joints. The second index avoids this potential problem by using only local information at the reference posture of the compliant mechanism. Here we describe the global structural error index (GSEI), which we believe is the ideal way to measure the level of nonlinearity.

2.1.1 GSEI. One of the most direct methods of quantifying the level of nonlinearity in Eq. (8) is through the root-mean-square value of the difference between $\bar{\mathbf{w}}(\hat{\mathbf{q}})$ and its own linear component, over the range $\mathbf{q}_{\min} \leq \mathbf{q} \leq \mathbf{q}_{\max}$ of measurable displacements. This may be expressed symbolically as

$$\sqrt{\int_0^1 \cdots \int_0^1 \|\bar{\mathbf{w}} - \dot{\mathbf{w}}\|^2 d\hat{q}_1 \cdots d\hat{q}_n} \quad (12)$$

In this expression, the estimated normalized force $\dot{\mathbf{w}}$ is obtained by linearizing $\bar{\mathbf{w}}(\hat{\mathbf{q}})$ about the reference posture $\hat{\mathbf{q}}_0$, which yields

$$\dot{\mathbf{w}} = \bar{\mathbf{H}}_0\mathbf{K}_q\hat{\mathbf{P}}^T(\hat{\mathbf{q}} - \hat{\mathbf{q}}_0) + \bar{\mathbf{H}}_0\mathbf{K}_q\check{\mathbf{P}}^T(\check{\mathbf{q}} - \check{\mathbf{q}}_0) + \bar{\mathbf{w}}_0 \quad (13)$$

where $\bar{\mathbf{H}}_0 \equiv \bar{\mathbf{H}}(\hat{\mathbf{q}}_0)$. The difference between the two vectors thus becomes

$$\bar{\mathbf{w}} - \dot{\mathbf{w}} = (\bar{\mathbf{H}} - \bar{\mathbf{H}}_0)\mathbf{K}_q\hat{\mathbf{P}}^T(\hat{\mathbf{q}} - \hat{\mathbf{q}}_0) + (\bar{\mathbf{H}} - \bar{\mathbf{H}}_0)\mathbf{K}_q\check{\mathbf{P}}^T(\check{\mathbf{q}} - \check{\mathbf{q}}_0) \quad (14)$$

In order to circumvent the problem of minimizing just the nonlinearity alone, we propose using the ratio of the nonlinearity error to the overall sensitivity of the compliant mechanism, both being measured by a root-mean-square computation, in order to formulate the index. This leads to the index

$$\gamma \equiv \frac{\sqrt{\int_0^1 \cdots \int_0^1 \|\bar{\mathbf{w}} - \dot{\mathbf{w}}\|^2 d\hat{q}_1 \cdots d\hat{q}_n}}{\sqrt{\int_0^1 \cdots \int_0^1 \|\bar{\mathbf{w}}\|^2 d\hat{q}_1 \cdots d\hat{q}_n}} \quad (15)$$

We refer to γ as the GSEI. In kinematic synthesis, the structural error indicates the deviation in the trajectory of the moving link of a mechanism, i.e., the deviation from the prescribed trajectory which the link was designed to follow. Here, γ measures the deviation of the mechanism from the ideal state, i.e., deviation from the state in which the Jacobian matrix remains constant. This deviation from the ideal state occurs with some mechanisms, especially those with highly nonrigid links. The term “global” here refers to the whole workspace in which the behavior of the compliant mechanism is being assessed, i.e., the workspace given by $\mathbf{q}_{\min} \leq \mathbf{q} \leq \mathbf{q}_{\max}$. Obviously, one may obtain the most accurate information by considering all the possible mechanism postures. However, this poses a computational problem, especially with six-axis force–torque sensors where one must evaluate a sextuple integral. A better alternative is a local index, as it only requires us to identify the behavior of the compliant mechanism at a single point.

2.1.2 Local Structural Error Index (LSEI). An efficient way to circumvent the computational burden of the GSEI (Eq. (15)) is to minimize the nonlinearity of Eq. (11) at the reference posture $\hat{\mathbf{q}}_0$. The ideal mechanical design for this index is the one for which an infinitesimal change of $\hat{\mathbf{q}}$ around the equilibrium configuration

will have the least effect on the changes in geometry. The instantaneous relationship between the normalized forces and the joint displacements can be found by differentiating Eq. (11), which yields

$$d\bar{\mathbf{w}} = d\bar{\mathbf{H}}\mathbf{K}_q \left(\hat{\mathbf{P}}^T (\hat{\mathbf{q}} - \hat{\mathbf{q}}_0) + \check{\mathbf{P}}^T (\check{\mathbf{q}} - \check{\mathbf{q}}_0) \right) + \bar{\mathbf{H}}\mathbf{K}_q \left(\hat{\mathbf{P}}^T d\hat{\mathbf{q}} + \check{\mathbf{P}}^T d\check{\mathbf{q}} \right) \quad (16)$$

Using the definition of $d\bar{\mathbf{H}}$, this equation can also be written as

$$d\bar{\mathbf{w}} = \left(\frac{\partial \bar{\mathbf{H}}}{\partial \hat{\mathbf{q}}} \Big|_0 \mathbf{K}_q \left(\hat{\mathbf{P}}^T (\hat{\mathbf{q}} - \hat{\mathbf{q}}_0) + \check{\mathbf{P}}^T (\check{\mathbf{q}} - \check{\mathbf{q}}_0) \right) + \bar{\mathbf{H}}_0 \mathbf{K}_q \right) \left(\hat{\mathbf{P}}^T d\hat{\mathbf{q}} + \check{\mathbf{P}}^T d\check{\mathbf{q}} \right), \quad (17)$$

where $(\partial \bar{\mathbf{H}} / \partial \hat{\mathbf{q}})|_0$ is a third-order tensor evaluated at the reference posture $\hat{\mathbf{q}} = \hat{\mathbf{q}}_0$. This expression is somewhat similar to the relation presented by Chen and Kao [20], in their work on the conservative congruence transformation of joint and Cartesian stiffness matrices. As they have proposed, one may expand Eq. (17) so as to avoid working with a third-order tensor. This leads us to

$$d\bar{\mathbf{w}} = \left(\left[\frac{\partial \bar{\mathbf{H}}}{\partial \hat{q}_1} \Big|_0 \mathbf{K}_q \left(\hat{\mathbf{P}}^T (\hat{\mathbf{q}} - \hat{\mathbf{q}}_0) + \check{\mathbf{P}}^T (\check{\mathbf{q}} - \check{\mathbf{q}}_0) \right) \quad \cdots \quad \frac{\partial \bar{\mathbf{H}}}{\partial \hat{q}_n} \Big|_0 \mathbf{K}_q \left(\hat{\mathbf{P}}^T (\hat{\mathbf{q}} - \hat{\mathbf{q}}_0) + \check{\mathbf{P}}^T (\check{\mathbf{q}} - \check{\mathbf{q}}_0) \right) \right] + \bar{\mathbf{H}}_0 \mathbf{K}_q \right) \left(\hat{\mathbf{P}}^T d\hat{\mathbf{q}} + \check{\mathbf{P}}^T d\check{\mathbf{q}} \right) \quad (18)$$

To retain just the nonlinear component of $d\bar{\mathbf{w}}$, we compare it against the (linearly) estimated normalized force $d\hat{\mathbf{w}}$, as expressed in Eq. (13). As the Jacobian matrix is a constant in this equation, taking the derivative on both sides simply yields

$$d\hat{\mathbf{w}} = \bar{\mathbf{H}}_0 \mathbf{K}_q \left(\hat{\mathbf{P}}^T d\hat{\mathbf{q}} + \check{\mathbf{P}}^T d\check{\mathbf{q}} \right) \quad (19)$$

Using this definition, the instantaneous distortion of the geometry due to an applied force can be expressed as

$$d\bar{\mathbf{w}} - d\hat{\mathbf{w}} = \left[\frac{\partial \bar{\mathbf{H}}}{\partial \hat{q}_1} \Big|_0 \mathbf{K}_q \left(\hat{\mathbf{P}}^T (\hat{\mathbf{q}} - \hat{\mathbf{q}}_0) + \check{\mathbf{P}}^T (\check{\mathbf{q}} - \check{\mathbf{q}}_0) \right) \quad \cdots \quad \frac{\partial \bar{\mathbf{H}}}{\partial \hat{q}_n} \Big|_0 \mathbf{K}_q \left(\hat{\mathbf{P}}^T (\hat{\mathbf{q}} - \hat{\mathbf{q}}_0) + \check{\mathbf{P}}^T (\check{\mathbf{q}} - \check{\mathbf{q}}_0) \right) \right] d\bar{\mathbf{q}} \quad (20)$$

where $d\bar{\mathbf{q}} = \hat{\mathbf{P}}^T d\hat{\mathbf{q}} + \check{\mathbf{P}}^T d\check{\mathbf{q}}$ and $d\check{\mathbf{q}} = d\bar{\mathbf{q}}(d\hat{\mathbf{q}})$. The magnitude $\|d\bar{\mathbf{w}} - d\hat{\mathbf{w}}\|_2$ of this distortion is to be minimized for all possible values of $\hat{\mathbf{q}}$ and $d\hat{\mathbf{q}}$.

As an alternative to a costly numerical integration of the possible combinations of these parameters, we elect to minimize an upper bound of $\|d\bar{\mathbf{w}} - d\hat{\mathbf{w}}\|_2$. To this end, let us define

$$\bar{\mathbf{F}} \equiv \left[\frac{\partial \bar{\mathbf{H}}}{\partial \hat{q}_1} \Big|_0 \mathbf{K}_q \quad \cdots \quad \frac{\partial \bar{\mathbf{H}}}{\partial \hat{q}_n} \Big|_0 \mathbf{K}_q \right] \quad (21)$$

$$\bar{\mathbf{Q}} \equiv \begin{bmatrix} \bar{\mathbf{q}} - \bar{\mathbf{q}}_0 & \mathbf{0}_n & \cdots & \mathbf{0}_n \\ \mathbf{0}_n & \bar{\mathbf{q}} - \bar{\mathbf{q}}_0 & \cdots & \mathbf{0}_n \\ \vdots & \vdots & \ddots & \vdots \\ \mathbf{0}_n & \mathbf{0}_n & \cdots & \bar{\mathbf{q}} - \bar{\mathbf{q}}_0 \end{bmatrix} \quad (22)$$

thus allowing Eq. (20) to be rewritten as

$$d\bar{\mathbf{w}} - d\hat{\mathbf{w}} = \bar{\mathbf{F}}\bar{\mathbf{Q}}d\bar{\mathbf{q}} \quad (23a)$$

Thence, the magnitude of the nonlinearity is bounded as

$$\|d\bar{\mathbf{w}} - d\hat{\mathbf{w}}\|_2 = \|\bar{\mathbf{F}}\bar{\mathbf{Q}}d\bar{\mathbf{q}}\|_2 \quad (23b)$$

$$\leq \|\bar{\mathbf{F}}\|_2 \|\bar{\mathbf{Q}}d\bar{\mathbf{q}}\|_2 \quad (23c)$$

$$\leq \|\bar{\mathbf{F}}\|_F \|\bar{\mathbf{Q}}d\bar{\mathbf{q}}\|_2 \quad (23d)$$

where $\|\cdot\|_F$ denotes the Frobenius norm. Notice that the last inequality was obtained from the relationship $\|\bar{\mathbf{F}}\|_2 \leq \|\bar{\mathbf{F}}\|_F$, which is true for any matrix $\bar{\mathbf{F}}$ (see Ref. [21]). In Eq. (23d), the compliant mechanism design parameters, that were captured in $\|\bar{\mathbf{F}}\|_F$, are decoupled from the displacements which appear in $\|\bar{\mathbf{Q}}d\bar{\mathbf{q}}\|_2$. Therefore, minimizing $\|\bar{\mathbf{F}}\|_F$ reduces the structural error of the mechanism without making any hypothesis on its displacements about the reference posture. We thus propose the following index as a local measure of the structural error:

$$\text{minimize } \lambda^2 \equiv \|\bar{\mathbf{F}}\|_F^2 \quad (24)$$

Accordingly, we refer to λ as the LSEI induced by a compliant mechanism. Notice that λ depends on the topology and dimensions of the rigid-link mechanism, as well as on the stiffnesses at its elastic joints and on its unloaded posture $\bar{\mathbf{q}}_0$. All these parameters may be considered as decision variables in problem (24).

For the purpose of optimization, it may prove useful to expand the expression of λ as

$$\begin{aligned}\lambda^2 &= \sum_{j=1}^n \left\| \frac{\partial \bar{\mathbf{H}}}{\partial \hat{q}_j} \right\|_0 \mathbf{K}_q \left\| \mathbf{F} \right\|^2 \\ &= \sum_{j=1}^n \text{tr} \left(\mathbf{K}_q^T \frac{\partial \bar{\mathbf{H}}^T}{\partial \hat{q}_j} \right)_0 \left(\frac{\partial \bar{\mathbf{H}}}{\partial \hat{q}_j} \right)_0 \mathbf{K}_q \\ &= \text{tr} \left(\mathbf{K}_q^T \left(\sum_{j=1}^n \frac{\partial \bar{\mathbf{H}}^T}{\partial \hat{q}_j} \right)_0 \left(\frac{\partial \bar{\mathbf{H}}}{\partial \hat{q}_j} \right)_0 \mathbf{K}_q \right) \\ &= \text{tr} \left(\mathbf{K}_q^2 \left(\sum_{j=1}^n \frac{\partial \bar{\mathbf{H}}^T}{\partial \hat{q}_j} \frac{\partial \bar{\mathbf{H}}}{\partial \hat{q}_j} \right)_0 \right)\end{aligned}\quad (25)$$

where these reformulations were allowed by the linearity of the trace operation and by its invariance under similarity transformations of its matrix argument. The expression obtained in Eq. (25) may provide the designer with more insight than could be obtained from Eq. (24) alone, as the stiffness parameters are factored from the geometric ones. Moreover, this formulation may prove more computationally efficient, as the stiffness \mathbf{K}_q^2 is only multiplied once, as compared to n times in the latter formula.

2.1.3 Validation. We will now perform a simple comparative analysis to verify the equivalence between the global and the LSEIs. Figure 3 shows the simple planar mechanism we chose to use for this demonstration. Following the definitions described above, we assign coordinate frames, lengths of rigid links, and joint variables, as shown in Fig. 3. The GSEI and LSEI are then formulated and computed for different values of $q_{0,1,2}$. The choice of computing only $q_{0,1,2}$ was motivated by the theory of serial mechanisms [19], since the first joint variable affects neither the Jacobian matrix of the mechanism, nor the indices derived from this matrix. A comprehensive comparison between the two indices yields the results of Fig. 4. It is clear from Fig. 4 that the curves of the two indices are quite similar, although they are on different scales. Note that these values could just as easily have been lower or higher, since both the GSEI and the LSEI are dimensionless (without a unit of measurement). Therefore, since the two indices result in a similar curve, it is better to use the local index, which is easily calculated, rather than the complex global one. One may also observe that the indices γ and λ with the lowest values correspond to the highest absolute values of $q_{0,1,2}$, i.e., to the design in which the mechanism is relatively far from the singularity.

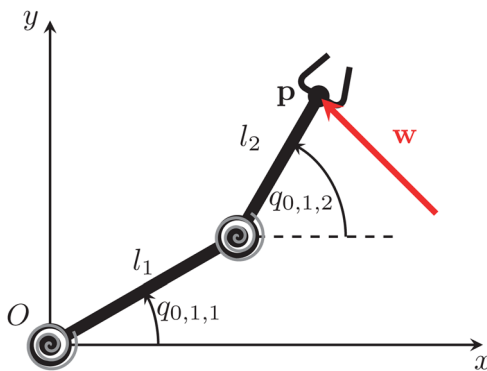


Fig. 3 Two-link planar compliant serial mechanism

This result is to be expected, as the theory discussed by Ref. [6] states that when a mechanism is close to singularity it requires only a small force to produce large displacements at the compliant joints; which significantly increases the changes in geometry.

2.2 Measurement Error Amplification Index (MEAI). As the displacement-sensor signal has a low amplitude, and is often analog, it is easily affected by errors. These errors can be classified into three main categories: (1) the noise from the high-frequency electromagnetic waves of electrical motors; (2) thermal drift; and (3) the errors caused by signal discretization. Let $\delta \bar{\mathbf{q}}$ be the error in $\bar{\mathbf{q}}$, and $\delta \bar{\mathbf{w}}$ be the error in $\bar{\mathbf{w}}$.

Our goal here is to quantify, with a single number, the amplification of the measurement error as it is transformed from the joint's displacement to wrench components. For this purpose, the linearized input-output relationship between $\dot{\bar{\mathbf{w}}}$ and $\bar{\mathbf{q}}$ given in Eq. (13) may be used, which yields

$$\delta \dot{\bar{\mathbf{w}}} = \bar{\mathbf{H}}_0 \mathbf{K}_q \delta \bar{\mathbf{q}} \quad (26)$$

The Euclidean norm of $\delta \dot{\bar{\mathbf{w}}}$, denoted $\| \delta \dot{\bar{\mathbf{w}}} \|$, is bounded as

$$\| \delta \dot{\bar{\mathbf{w}}} \| \leq \| \bar{\mathbf{H}}_0 \mathbf{K}_q \| \| \delta \bar{\mathbf{q}} \| \quad (27)$$

where $\| \bar{\mathbf{H}}_0 \mathbf{K}_q \|$ is the matrix norm of its argument. Again, from Eq. (13), we isolate $\bar{\mathbf{q}} - \bar{\mathbf{q}}_0$, which gives

$$\bar{\mathbf{q}} - \bar{\mathbf{q}}_0 = (\bar{\mathbf{H}}_0 \mathbf{K}_q)^{-1} (\dot{\bar{\mathbf{w}}} - \bar{\mathbf{w}}_0) \quad (28)$$

From Eq. (28), $\| \bar{\mathbf{q}} - \bar{\mathbf{q}}_0 \|$ is bounded as

$$\| \bar{\mathbf{q}} - \bar{\mathbf{q}}_0 \| \leq \| (\bar{\mathbf{H}}_0 \mathbf{K}_q)^{-1} \| \| \dot{\bar{\mathbf{w}}} - \bar{\mathbf{w}}_0 \| \quad (29)$$

From Eqs. (27) and (29), we obtain

$$\frac{\| \delta \dot{\bar{\mathbf{w}}} \|}{\| \dot{\bar{\mathbf{w}}} - \bar{\mathbf{w}}_0 \|} \leq \| \bar{\mathbf{H}}_0 \mathbf{K}_q \| \cdot \| (\bar{\mathbf{H}}_0 \mathbf{K}_q)^{-1} \| \frac{\| \delta \bar{\mathbf{q}} \|}{\| \bar{\mathbf{q}} - \bar{\mathbf{q}}_0 \|}$$

Finally, the maximum ratio of the relative error in $\bar{\mathbf{w}}$, divided by ratio of the relative error in $\bar{\mathbf{q}}$, may be rewritten as

$$\frac{\| \delta \dot{\bar{\mathbf{w}}} \|}{\| \dot{\bar{\mathbf{w}}} - \bar{\mathbf{w}}_0 \|} \leq \kappa \frac{\| \delta \bar{\mathbf{q}} \|}{\| \bar{\mathbf{q}} - \bar{\mathbf{q}}_0 \|} \quad (30)$$

where κ is the product of the norms

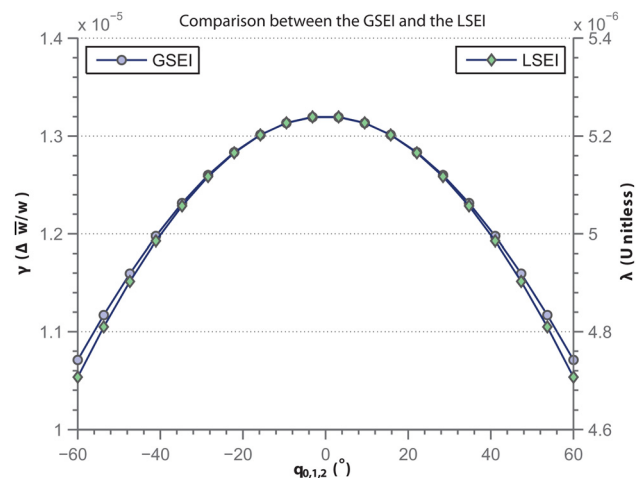


Fig. 4 Comparison between the global and local indices of structural error

Table 1 Optimization results for the two-link planar mechanism

\mathbf{x}	$q_{0,1,1}$ rad	$q_{0,1,2}$ rad	l_1 mm	l_2 mm	$k_{1,1}$ N m/rad	$k_{1,2}$ N m/rad	$1 - \frac{1}{\kappa}$ NA	λ NA
\mathbf{x}_{\min}	0	-1.57	10	10	1	1	NA	NA
\mathbf{x}_{\max}	3.14	1.57	60	60	687	687	NA	NA
\mathbf{x}_0	Initial parameter settings, selected by estimation							
	2.59	0.12	44.8	17.3	305	74.2	0.99	4.9×10^{-4}
	2.37	-0.7	35.3	34.6	112	82.72	0.88	1.6×10^{-4}
	2.37	-0.7	35.3	34.6	112	82.72	0.88	1.6×10^{-4}
$\alpha = 0$	2.59	1.57	60	10	112	684	0.15	18.9×10^{-5}
$\alpha = 0$	2.37	-1.57	60	10	31.6	192	0.15	1.4×10^{-5}
$\alpha = 0.83$	2.37	-1.57	12.3	10	112	82.7	0.67	10.5×10^{-6}

$$\kappa = \|\bar{\mathbf{H}}_0 \mathbf{K}_q\| \|(\bar{\mathbf{H}}_0 \mathbf{K}_q)^{-1}\| = \frac{\sigma_{\max}(\bar{\mathbf{H}}_0 \mathbf{K}_q)}{\sigma_{\min}(\bar{\mathbf{H}}_0 \mathbf{K}_q)} \quad (31)$$

According to Eq. (30), the noise $\delta \bar{\mathbf{q}}$ can affect $\bar{\mathbf{w}}$ through the matrix $\bar{\mathbf{H}}_0 \mathbf{K}_q$. The condition number κ measures the upper bound of the relative-error amplification. From this observation, one may consider the condition number as an objective function to be minimized. In order to keep the corresponding index between zero and one, we instead choose the objective

$$1 - \frac{1}{\kappa} \quad (32)$$

which is to be minimized. We refer to this index as the MEAI. The MEAI corresponds to the variation in the relative-error amplification, and may be expressed as

$$1 - \frac{1}{\kappa} = \frac{\sigma_{\max} - \sigma_{\min}}{\sigma_{\max}} \quad (33)$$

3 Multi-Objective Optimization

Not being completely satisfied with our formulation of the performance indices, let us propose a systematic optimization method which aims to guarantee the best possible design for a force–torque sensor. Since we have established in this study that both the LSEI and the MEAI are the main performance indicators of the sensor design, it is essential to consider both indices simultaneously in order to overcome the problems of mono-objective

optimization. Note that the GSEI has not been used, due to its computational burden, as explained previously. Section 4 shows how our proposed multi-objective optimization method may be used to find the optimal design parameters for a compliant mechanism-based force–torque sensor.

3.1 Formulation of the Optimization Problem. Typically in multi-objective problems, any advance made toward one objective will inevitably be offset by a decrease in the functioning of another objective. There are several techniques available for solving multi-objective optimization problems, but we have chosen to use the concept of global weighted sum, also called Pareto optimality [22].

Let us first turn our attention toward the combination of the LSEI and the MEAI using Pareto optimization. We consider the indices in Eqs. (25) and (32) as objective functions, each weighted by a coefficient α . Therefore, the optimization problem is concerned with the minimization of the new objective function $f(\mathbf{x}, \alpha)$ that can be subject to a number of constraints and bounds. The problem may be expressed as follows:

$$\min_{\mathbf{x} \in \mathbb{R}} f(\mathbf{x}, \alpha) = \alpha \lambda + (1 - \alpha) \left(1 - \frac{1}{\kappa}\right) \quad (34a)$$

$$g(\mathbf{x}) = 0 \quad (34b)$$

$$g(\mathbf{x}) \leq 0 \quad (34c)$$

$$\mathbf{x}_{\min} \leq \mathbf{x} \leq \mathbf{x}_{\max} \quad (34d)$$

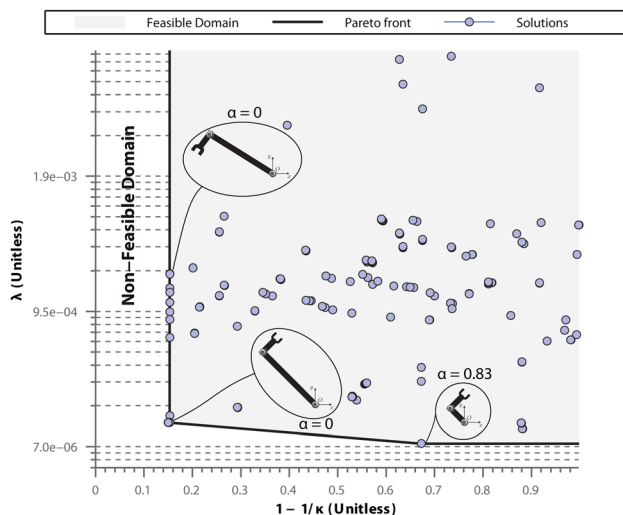


Fig. 5 Results of Pareto optimization for the two-link planar mechanism

Solving the problem (34) for several values of α (knowing that α varies between zero and one) allows us to compare solutions based on different initial scenarios. In fact, the minimum values of LSEI and MEAI occur when $\alpha = 1$ and $\alpha = 0$, respectively. All values in-between represent a tradeoff between the objectives, so it is up to the designer to select the solution that will best fit within the constraints imposed by the technical specifications. Given that the choice of the vector of the design parameters \mathbf{x} is arbitrary, nothing guarantees that the allowed range of measured joint displacements will match the range of applied wrenches. Thus, the constraints in Eq. (34b) to Eq. (34d) can be used to scale the input and output of Eq. (11). In MATLAB[®], we solved the constrained nonlinear optimization problem using the *fmincon* command. This command prompts the sequential quadratic programming routine of MATLAB[®] which is used to implement the Pareto optimization procedure.

4 Case Study: Optimization Procedure Applied to a Serial Two-Link Mechanism

To illustrate the core ideas of this paper, this section will show how the optimization procedure may be applied to the structural dimensioning of a compliant-serial mechanism. Here we present

our evaluation of the performance of a two-link planar mechanism with two pivot joints. As this is the simplest type of multijoint serial mechanism, obviously it will not be used as a compliant mechanism at the core of a real force sensor. Nevertheless, this example serves to provide a simplified illustration of the proposed design method.

4.1 Mechanism Description and Kinematics. The proposed serial mechanism, with two degrees-of-freedom, is shown in Fig. 3, where the point of force application is denoted $\mathbf{p}(x, y)$. Likewise, the position of the joints is indicated by $\mathbf{q} = [q_{0,1,1}, q_{0,1,2}]^T$. We consider the joint stiffness matrix \mathbf{K}_q to be a diagonal matrix. In this example, the vector of maximum applied wrench is $\mathbf{w}_{\max} = [5, 5]$ N, the vector of minimum applied wrench is $\mathbf{w}_{\min} = [-5, -5]$ N, and the range of joint displacements extends from -0.3 rad to $+0.3$ rad (i.e., $\Delta\hat{q} = 0.6$ rad).

We must place limits on the design parameters to avoid impractical solutions. These boundaries, and other details of the optimization problem, are presented in Table 1. Our objective is to find the set of design parameters of interest $\mathbf{x} = [q_{0,1,1}, q_{0,1,2}, l_1, l_2, k_{1,1}, k_{1,2}]^T$ that minimize the objective function given in Eq. (34a).

4.2 Optimization Results for the Serial Two-Link Mechanism. The indices presented in Eqs. (25) and (32) can be formulated using the Jacobian matrix involved in the kinematic equations of the two-link serial mechanism [23]. The resulting formulas are then used to solve the optimization problem (34). Figure 5 shows the Pareto front obtained from a logarithmically spaced sequence of α and several randomly generated initial guesses. We observe from Fig. 5 that by properly modulating the input design parameters, both the LSEI and MEAI have improved, as $1 - 1/\kappa$ ranges from 0.15 to 1 and λ ranges from 1.05×10^{-5} to 7.6×10^{-3} . Due to the large number of possible solutions, we focus on the three most promising designs. These are shown in Fig. 5 and compared in Table 1. The first and second scenarios result in solutions where only $1 - 1/\kappa$ is minimized (i.e., $\alpha = 0$). We found that the minimum of the MEAI exists at design solutions where the ratio $l_1 : l_2$ is highest, and $q_{0,1,2}$ is equal to ± 90 deg. The third scenario represents an intermediate Pareto optimal solution, since both indices have improved relative to the indices generated by the initial guesses. In this case, the minimum of the LSEI and the MEAI occurs at design solutions where the ratio $l_1 : l_2$ is lowest. Thus, from a practical perspective, this design has a better geometry because it makes the force sensor compact and easy to fabricate. One may also observe from Table 1 that the only components that vary with optimization are $q_{0,1,2}$ —i.e., the joint stiffnesses and the link lengths—whereas $q_{0,1,1}$ remains constant. This observation is consistent with the theory of serial mechanisms [19], as explained previously.

5 Case study: Application to the 2-PRR Planar Force Sensor

This section first presents a 2-PRR compliant parallel mechanism-based force sensor, including the mechanism principle and kinematics, in order to show the versatility of the proposed design method. It will then display the contour plots of the proposed performance indices. Finally, the results for the optimized 2-PRR compliant mechanism are depicted and discussed.

5.1 Sensor Description and Kinematics. As a practical example, consider the design of a planar multi-axis force sensor for measurement of the force $\mathbf{w} \in \mathbb{R}^2$, as illustrated in Fig. 6. The compliant mechanism of this force sensor will allow for planar displacements at the position of joint q_3 , represented by $\mathbf{p} \equiv [x, y]^T$. Displacements will only take place on the x - y plane, as the joint is too stiff to allow displacements in other directions.

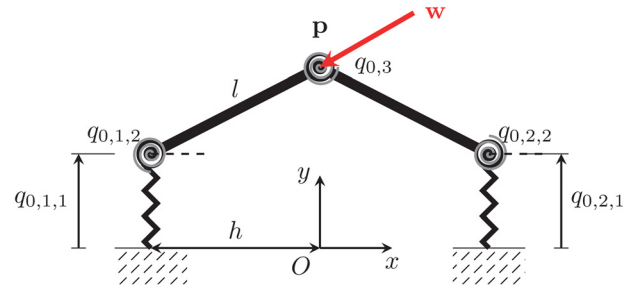


Fig. 6 A 2-PRR planar biaxial force sensor mechanism

Therefore, the compliant mechanism can simply be modeled as the lumped-elastic parallel mechanism of Fig. 6.

According to this model, the point of application of the force is connected to the frame by two PRR-type legs. Each pivot joint is coupled with a torsion spring, and each prismatic joint with a linear spring. We assume the architecture of the mechanism to be symmetrical. Let us define the vectors $\mathbf{q}_i \equiv [q_{i,1}, q_{i,2}]^T$, $i = 1, 2$, representing the joint displacements; the vector $\hat{\mathbf{q}} \equiv [q_{1,1}, q_{2,1}]^T$, representing the measured joint variables; the vector $\tilde{\mathbf{q}} \equiv [q_{1,2}, q_{2,2}]^T$, representing the unmeasured joint variables; and the vector $\mathbf{q}_0 \equiv [q_{0,1,1} \cdots q_{0,2,2}]^T$, representing the free lengths of the corresponding springs.

It is more complex to compute the stiffness matrix \mathbf{K}_q , due to the presence of a fifth spring located between the two bars connected at \mathbf{p} . This spring is of stiffness k_3 and free-length $q_{0,3}$, and its elongation is given by $q_3 - q_{0,3}$, where $q_{0,3}$ is the angle between the two bars. As this angle depends upon $q_{0,1,2}$ and $q_{0,2,2}$, it was excluded from the vectors \mathbf{q} and \mathbf{q}_0 . Thus, the contribution of the spring k_3 to the matrix of stiffness is $\mathbf{k} = [k_{1,1}, k_{1,2} + k_3, k_{2,1}, k_{2,2} + k_3]^T$, where $\mathbf{K}_q \equiv \text{diag}(\mathbf{k})$.

The inverse kinematic problem of this mechanism consists in expressing the free lengths of the measured joint displacements $\hat{\mathbf{q}}_0 = [q_{0,1,1}, q_{0,2,1}]^T$ as functions of the position $\mathbf{p} = [x, y]^T$ of application of the force \mathbf{w} . We refer the reader to Ref. [7] for the complete derivation. As the purpose of this paper is not to discuss the full details of the kinematics, we present only the solution to the inverse kinematic problem

$$\begin{aligned} q_{0,1,1} &= y \pm \sqrt{(l^2 - (x + h)^2)} \\ q_{0,2,1} &= y \pm \sqrt{(l^2 - (x - h)^2)} \end{aligned} \quad (35)$$

where h is the distance between the center of the base frame and the axis passing through the fixed linear joint. The symbol \pm in the system of Eq. (35) indicates the four possible sets of solutions to this problem. For the purpose of this example, we retain only the solutions that correspond to the negative branches of Eq. (35), i.e., those postures where $q_{0,1,1} \leq y$ and $q_{0,2,1} \leq y$.

5.2 Performance Indices of the 2-PRR Planar Force Sensor. One way to easily infer the critical behavior of the indices at specific geometries is to trace the contours of the proposed performance indices over a two-dimensional design space. Figure 6 shows that nine variables can be admitted as design parameters: $q_{0,1,1}$, $q_{0,2,1}$, l , h , $k_{1,1}$, $k_{1,2}$, $k_{2,1}$, $k_{2,2}$, and k_3 . These variables may each have a significant impact on the force-displacement relation of Eq. (11). Computing and tracing the relationships between the three indices and all nine design parameters is tedious and impractical. Therefore, we initially restrict ourselves to the consideration of just two of them at a time. For example, let us determine the values of $q_{0,1,1}$ and $q_{0,2,1}$ that will result in the best possible design.

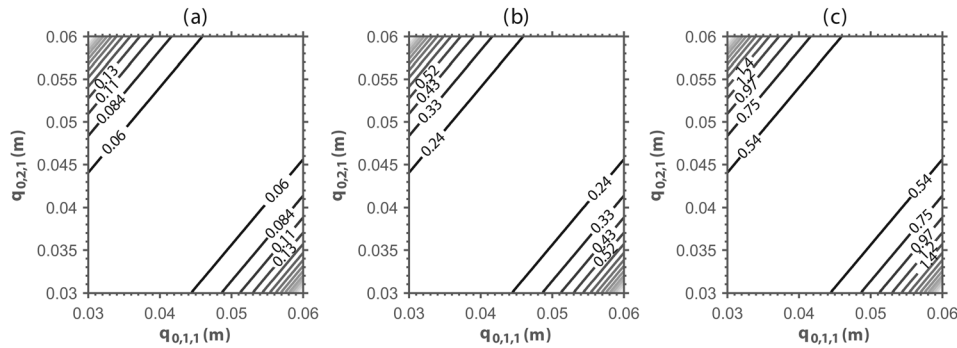


Fig. 7 Comparison of the contour plots of the GSEI for the 2-PRR mechanism: (a) $d\hat{q} = 0.3$ mm, (b) $d\hat{q} = 0.6$ mm, and (c) $d\hat{q} = 0.9$ mm

We assume that the measured joint variables $q_{0,1,1}$ and $q_{0,2,1}$ vary from 30 mm to 60 mm, and that the mechanism has a symmetric stiffness matrix, i.e., $k_{1,1} = k_{2,1}$ and $k_{1,2} = k_{2,2}$. The remaining parameters are set to: $l = 40$ mm, $h = 25$ mm, $k_{1,1} = k_{2,1} = 9.66 \times 10^3$ N/m for the linear joints, and $k_{1,2} = k_{2,2} = 33.7$ N m/rad for the angular joints. As stated in Sec. 2, the designer knows in advance that the variation in the position of the vector $\hat{\mathbf{q}}$ with respect to $\hat{\mathbf{q}}_0$ is equal to the maximum deformations allowed at the compliant measured joints. Therefore, the vector $\Delta\hat{\mathbf{q}} = \hat{\mathbf{q}} - \hat{\mathbf{q}}_0$ is equal to the range of the sensor that is placed on the relevant joint. For example, if the joint's range of motion, $q_{1,1}$, extends from -0.3 mm to $+0.3$ mm, then $\Delta\hat{q} = 0.6$ mm. In addition, the vectors of the minimum and maximum applied wrenches are, respectively, $\mathbf{w}_{\min} = [-5 \ -5]$ N and $\mathbf{w}_{\max} = [5 \ 5]$ N.

Having defined the parameters, we will now compute the index γ from Eq. (15). This is calculated three times along 50×50 grids, according to three separate assumptions regarding the ranges of joint displacements: $\Delta\hat{q} = 0.3$ mm, $\Delta\hat{q} = 0.6$ mm, and $\Delta\hat{q} = 0.9$ mm. Figure 7 depicts the resulting contour plots of each γ index, showing how the index relates to the level of $\Delta\hat{q}$. As can be seen, the index γ with the lowest value corresponds to the lowest value of $\Delta\hat{q}$, i.e., to the design in which the measured joints exhibits the least displacement magnitude. This result is to be expected, as the theory discussed earlier states that a smaller range of the joint displacements values results in lower values of the GSEI.

The next step is to generate three separate performance indices and transform them into Cartesian space for simple visualization. We used the method described in the previous paragraph to calculate the values of three separate indices in the joint space. From Eqs. (15), (25), and (32), we can compute γ , λ , and $1 - 1/\kappa$ for the 2-PRR mechanism according to the design parameters specified above. These were then transformed into Cartesian space

using inverse kinematics, to obtain the contour plots of the GSEI, the LSEI, and the MEAI.

Based on the simulation results, we can now compare the three indices to determine which design performs best. From Figs. 8(a) and 8(b), one may observe that the contour lines of γ are quite similar to those of λ . Therefore, the use of one of these contours instead of the other to select the values of x and y does not affect the final design, except that the values of λ are proportionally higher than those of γ . In regard to Fig. 8(c), one may observe that the contour lines of $1 - 1/\kappa$ are also similar to those of the GSEI and the LSEI. Nevertheless, the LSEI cannot be replaced by the MEAI since the latter does not take into account the properties of the springs attached to the unmeasured joint of the compliant mechanism. Section 5.3 of this paper will present a follow-up to this analysis. We will describe how the optimization procedure shown in Sec. 3 can be used to further improve the performance indices when optimizing several parameters at once.

5.3 Optimization Results for the 2-PRR Planar Force Sensor. In this section, we examine how the performance of the 2-PRR compliant mechanism can be improved when the rest of the design parameters are included as part of the optimization process. For this purpose, the design parameters are optimized to improve both the LSEI and the MEAI according to the problem of Eq. (34). As previously mentioned, the parameters are grouped in the vector $\mathbf{x} = [q_{0,1,1}, q_{0,2,1}, l, h, k_{1,1}, k_{1,2}, k_3]$, and we assume $k_{1,1} = k_{2,1}$ and $k_{1,2} = k_{2,2}$. Also, as in Sec. 5.2, the vectors of minimum and maximum applied wrenches are, respectively, $\mathbf{w}_{\min} = [-5 \ -5]$ N and $\mathbf{w}_{\max} = [5 \ 5]$ N, and the range of measured joint displacements is $\Delta\hat{q} = 0.6$ mm. Again, we must place limits on the design parameters to avoid impractical solutions. These boundaries, and other details of the optimization problem, are presented in Table 2.

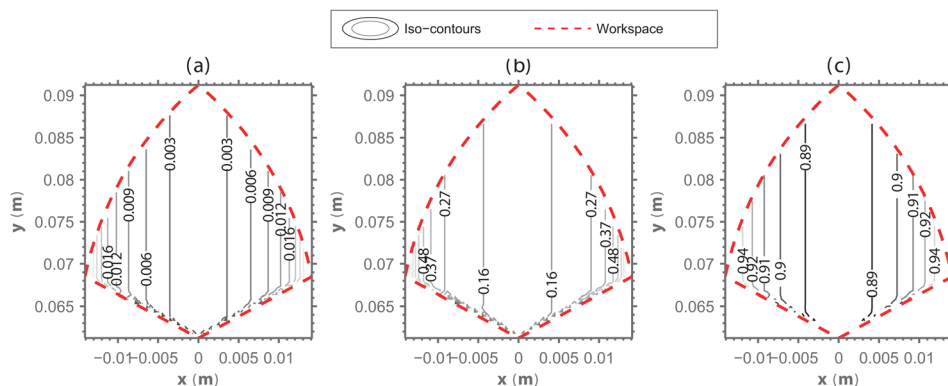


Fig. 8 Contour plots in Cartesian space of the performance indices for the 2-PRR mechanism: (a) GSEI, (b) LSEI, and (c) MEAI

Table 2 Results of the optimization process for the 2-PRR planar mechanism

\mathbf{x}	$q_{0,1,1}$ mm	$q_{0,2,1}$ mm	l mm	h mm	$k_{1,1}$ N/m	$k_{1,2}$ N m/rad	k_3 N m/rad	$1 - 1/\kappa$ NA	λ NA
\mathbf{x}_{\min}	35	35	40	25	1.66	1	1	NA	NA
\mathbf{x}_{\max}	50	50	60	39	9.6×10^3	687	687	NA	NA
\mathbf{x}_0	Initial parameter settings, selected by estimation								
	39	45	51.3	27	2.08×10^3	1.48	1.12	0.22	6.2×10^{-3}
	35	38	52.1	37.2	6.18×10^3	12.37	4.35	0.55	25.8×10^{-3}
	40.3	41.7	47.3	26.5	3.19×10^3	1.24	4.12	0.43	11.6×10^{-3}
$\alpha = 0.60$	35	35	60	30.6	2.08×10^3	1.36	1.28	1.81×10^{-6}	5.3×10^{-3}
$\alpha = 0.37$	35	35	60	26.1	6.18×10^3	6.63	1.00	1.33×10^{-7}	1.72×10^{-2}
$\alpha = 0$	35	35	60	32.9	3.19×10^3	1.08	2.89	2.21×10^{-7}	8.02×10^{-3}

Because we wish to minimize both the LSEI and the MEAI, the optimization problem is multi-objective. We thus expect to obtain several optima corresponding to as many values of α in problem (34). Figure 9 presents the solutions obtained from a logarithmically spaced sequence of α and 50 randomly generated initial guesses. The boundary of the 8750 ensuing solutions approximates the Pareto front. We believe that these solutions cover the seven-dimensional design space sufficiently well for our purpose. The fact that the cloud of initial guesses resulted in a cloud of optimized solutions in the southwest area of the graph shows that we were able to generate many improved solutions within our design constraints. Ultimately, λ reaches a minimum value of 5.2×10^{-3} , and $1 - 1/\kappa$ reaches a minimum value of 8.7×10^{-8} . The latter value corresponds to the condition number of one (an isotropic design), although as of yet we have not found one design that obtains precisely these two minima at the same time.

Each solution on the Pareto front represents the parameters that optimize a certain weighted sum of different functions for the design of the compliant mechanism. Examples of possible design

solutions are given in Table 2, along with their corresponding performance indices λ and $1 - 1/\kappa$. The different solutions found on the Pareto front actually result in the same values for some of the corresponding design parameters. For instance, all the solutions shown on the Pareto front require the same design parameters: the geometry of the mechanism must be symmetric, i.e., $q_{0,1,1} = q_{0,2,1}$, and the ratio between the parameters l and h , if found, is approximately 1:2. The obtained stiffnesses indicate that in all three cases, the rigidity of the compliant mechanism will vary with the values of the performance indices. This means it is important to consider both the optimization of the topology, and the rigidity of the mechanism's structure. Note also that the obtained design parameters when $\alpha = 0.6$ produces a compliant mechanism that shows the most linear behavior in response to large changes in joint displacement. This means that in practical conditions, the estimated forces will be far more accurate than the estimated forces that would be obtained from the other designs. Of course, for our force sensor, each solution is the result of a trade-off between the sensor's sensitivity to noise from the

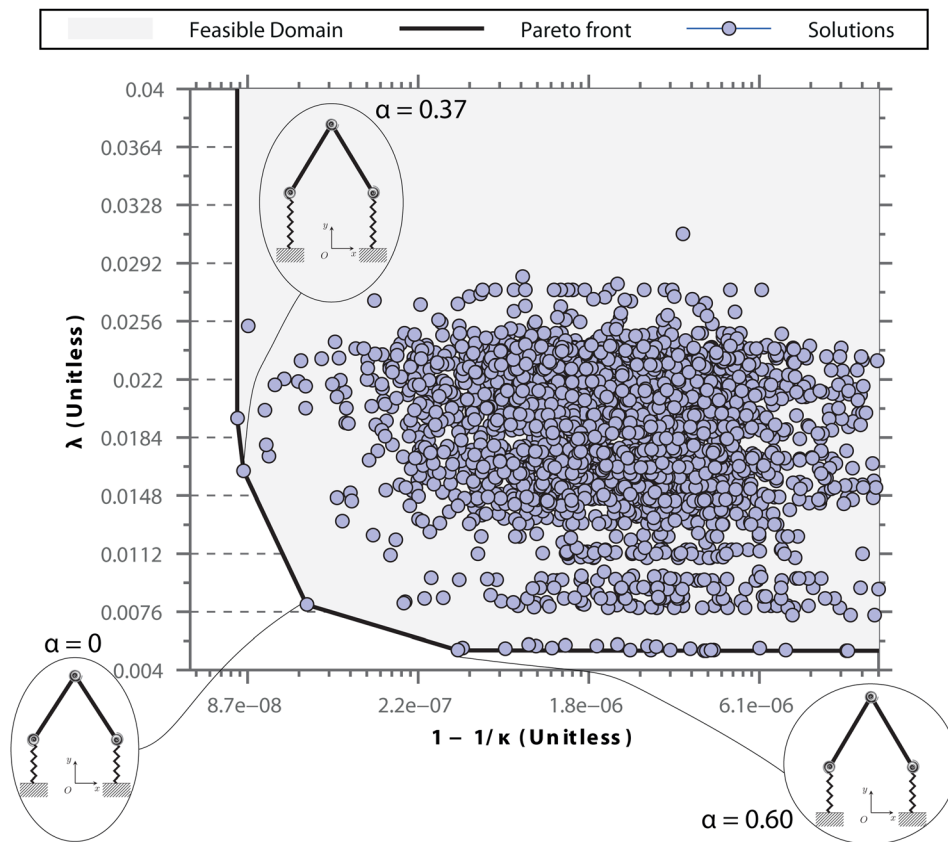


Fig. 9 Pareto optimization for the 2-PRR planar mechanism: close-up view of the concentration of solutions at the Pareto front

displacement sensors, and its sensitivity to nonlinearities resulting from changes in geometry. Therefore, the decision to optimize one of these functions, at the expense of the other, ultimately rests with the designer.

6 Conclusion

In this paper, we have proposed and validated a novel method of designing the compliant mechanism that forms the core of force–torque sensors. More specifically, we have used the kineto-static relationship between applied wrench and measured joint displacements to formulate several indices. These indices are used in the multi-objective optimization process, based on Pareto-optimization, to find the best design. Assuming that the compliant mechanism can be modeled as a lumped compliance rigid-link mechanism, these performance indices can be applied to any sensor mechanism, allowing us to quantify the structural error using the GSEI or LSEI, and to quantify the measurement error amplification using the MEAI. The most important aspects of the performance indices are summarized as follows:

- (1) The indices take several variables into account, allowing the designer to obtain a sensor that meets the specifications he or she desires.
- (2) However, since the indices are based on the wrench-displacement relationship, it is relatively complex to compute the indices for any mechanism with six degrees-of-freedom.
- (3) Finally, the indices apply to any compliant mechanism, kinematically redundant or not.

In order to illustrate the applicability of the proposed design method, we applied it to a 2-link compliant-serial mechanism and a 2-PRR compliant-parallel mechanism. The results show that the optimization process does improve the indices, and in theory, the design. However, to fully validate the indices, we must manufacture the mechanisms, test them, and determine whether they are indeed optimal designs.

References

- [1] Marín, R., Sanz, J.-P., and Schilling, K., 2004, *Methodology and Tools in Telemanipulation Systems Via Internet*, Universitat Jaume I, Castellon, Spain.
- [2] Rosen, J., Hannaford, B., and Satava, M.-R., 2011, *Surgical Robotics: Systems Applications and Visions*, Springer, New York.

- [3] González, I.-A., Fernández, M., Maestre, J.-M., and María a del Pilar, A.-G., 2011, *Service Robotics Within the Digital Home: Applications and Future Prospects*, Springer, The Netherlands.
- [4] Svinin, M., and Uchiyama, M., 1995, "Optimal Geometric Structures of Force/Torque Sensors," *Int. J. Rob. Res.*, **14**(6), pp. 560–573.
- [5] Dwarakanath, T.-A., Dasgupta, B., and Mruthyunjaya, T.-S., 2001, "Design and Development of a Stewart Platform Based Force-Torque Sensor," *Mechatronics*, **11**(7), pp. 793–809.
- [6] Ranganath, R., Nair, P.-S., Mruthyunjaya, T.-S., and Ghosal, A., 2004, "A Force-Torque Sensor Based on a Stewart Platform in a Near-Singular Configuration," *Mech. Mach. Theory*, **39**(9), pp. 971–998.
- [7] Merlet, J.-P., 1997, *Parallel Robots*, HERMES Science, Houten, The Netherlands.
- [8] Uchiyama, M., and Hakomori, K., 1985, "A Few Considerations on Structural Design of Force Sensors," 3rd Annual Conference on Japan Robotics Society, pp. 17–18 (in Japanese).
- [9] Uchiyama, M., Bayo, E., and Palma-Villalon, E., 1988, "A Mathematical Approach to the Optimal Structural Design of a Robot Force Sensor," USA-JAPAN Symposium on Flexible Automation, Vol. 1, pp. 539–546.
- [10] Bicchi, A., 1992, "A Criterion for Optimal Design of Multi-Axis Force Sensors," *J. Rob. Auton. Syst.*, **10**(4), pp. 269–286.
- [11] Bekhti, R., Duchaine, V., and Cardou, P., 2014, "Structural Optimisation of a Force-Torque Sensor Through its Input-Output Relationship," *Trans. Can. Soc. Mech. Eng.*, **38**(2), pp. 199–212.
- [12] Hirose, S., and Yoneda, K., 1990, "Development of Optical 6-Axial Force Sensor and its Signal Calibration Considering Non-Linear Interference," *IEEE International Conference on Robotics and Automation*, Cincinnati, OH, May 13–18, pp. 46–53.
- [13] Gogu, G., 2008, *Structural Synthesis of Parallel Robots, Part 1: Methodology*, Vol. 1, Springer, The Netherlands.
- [14] Hirzinger, G., and Dietrich, J., 1986, "Multisensory Robots and Sensorbased Path Generation," *IEEE International Conference on Robotics and Automation*, pp. 1992–2001.
- [15] Piller, G., 1982, "A Compact Six Degree-of-Freedom Force Sensor for Assembly Robot," 12th International Symposium on Industrial Robots, pp. 121–129.
- [16] Kang, C.-G., 2001, "Closed-Form Force Sensing of a 6-Axis Force Transducer Based on the Stewart Platform," *Sens. Actuators, A*, **90**(1–2), pp. 31–37.
- [17] Kvasnica, M., 1992, "Six-Component Force-Torque Sensing by Means of One Square CCD or PSD Element," *International Symposium on Measurement and Control in Robotics*, pp. 213–219.
- [18] Salisbury, J.-K., 1980, "Active Stiffness Control of a Manipulator in Cartesian Coordinates," 19th *IEEE Conference on Decision and Control* Including the Symposium on Adaptive Processes, Albuquerque, NM, Dec. 10–12, Vol. 19, pp. 95–100.
- [19] Yoshikawa, T., 1985, "Manipulability of Robotic Mechanisms," *Int. J. Rob. Res.*, **4**(2), pp. 3–9.
- [20] Kao, I., and Chen, S.-F., 2000, "Conservative Congruence Transformation for Joint and Cartesian Stiffness Matrices of Robotic Hands and Fingers," *Int. J. Rob. Res.*, **19**(9), pp. 835–847.
- [21] Golub, G., and Van Loan, C., 1996, *Matrix Computations*, Johns Hopkins University, Baltimore, MD.
- [22] Censor, Y., 1977, "Pareto Optimality in Multiobjective Problems," *Appl. Math. Optim.*, **4**(1), pp. 41–59.
- [23] McCarthy, J.-M., 1990, *An Introduction to Theoretical Kinematics*, Vol. 1, MIT, Cambridge, MA.